First Measurements of Rayleigh-Taylor-Induced Magnetic Fields in Laser-Produced Plasmas

M. J.-E. Manuel, C. K. Li, F. H. Séguin, J. Frenje, D. T. Casey, R. D. Petrasso, S. X. Hu, R. Betti, J. D. Hager, D. D. Meyerhofer, and V. A. Smalyuk

First Measurements of Rayleigh-Taylor-Induced Magnetic Fields in Laser-produced Plasmas

M. J.-E. Manuel, C. K. Li, F. H. Séguin, J. Frenje, D. T. Casey, and R. D. Petrasso

Plasma Science and Fusion Center, Massachusetts Institute of Technology, Cambridge, MA

S. X. Hu, R. Betti,* J. D. Hager,[†] D. D. Meyerhofer,* and V. A. Smalyuk[‡]

Laboratory for Laser Energetics, University of Rochester, Rochester, NY

(Dated: April 26, 2012)

The first experimental demonstration of Rayleigh-Taylor-induced magnetic fields due to the Biermann battery effect has been made. Experiments with laser-irradiated plastic foils were performed to investigate these illusive fields using a monoenergetic proton radiography system. Path-integrated B-field strength measurements were inferred from radiographs and found to increase from 10 to 100 Tesla-μm during the linear growth phase for 120 μm perturbations. Proton fluence modulations were corrected for Coulomb scattering using measured areal density profiles from X ray radiographs.

PACS numbers: 52.30.-q, 52.35.-g, 07.55.Db

A hydrodynamic system in which the density gradient opposes the acceleration (g) is susceptible to the Rayleigh-Taylor [1, 2] (RT) instability. This configuration occurs in many systems: in laser-matter interactions [3], during the acceleration and deceleration phases in inertial confinement fusion (ICF) [4], during core-collapse of supernovae [5], in stellar coronae [6], and in other astrophysical phenomena. In these systems, the fluids undergoing the instability are plasmas where separate ion and electron populations within the fluid can be affected by magnetic fields applied externally, or generated internally. The so-called Biermann battery [7] is the dominant source of self-generated magnetic fields in plasmas. This source term has been predicted to cause field generation due to the RT instability in astrophysical contexts [8] as well as in laser-plasma interactions [9–11]. In this letter, the first measurements of RT-induced magnetic fields due to the Biermann battery effect are presented and results discussed.

Experiments were performed on the OMEGA laser [12] using the setup shown in Figure 1a. CH foils, 21±2 μm thick, were seeded with 2D sinusoidal perturbations of wavelength λ=120±2 μm and amplitude a_0=0.27±0.02 μm. Twelve OMEGA beams were overlapped to ablatively drive modulated foils over a 2 ns square pulse providing an intensity of ∼4×10^{14} W/cm^2 in a ∼800 μm diameter spot. To provide uniform illumination across the target, beams were smoothed by spectral dispersion [13] (SSD) and distributed polarization rotators [14] (DPRs). The intensity profiles were shaped using SG4 distributed phase plates [15] (DPPs). In proton backlighting experiments, D^{3}He protons are deflected in the target by field and mass modulations as shown in Figure 1b. The strength of path-integrated mass and fields, as illustrated in Figure 1c, determines the amount of proton deflection.

During the ablation process, dynamic charge separation and subsequent current generation will create electromagnetic fields [16–18] within the plasma. Ignoring electron inertia, the equations governing self-generated **B** and **E** fields can be written as

$$\frac{\partial \mathbf{B}}{\partial t} \approx \nabla \times \left(\frac{\nabla p_e}{en_e} \right) + \nabla \times (\mathbf{v} \times \mathbf{B}) \ , \tag{1}$$

$$\mathbf{E} \approx -\frac{\nabla p_e}{en_e} - \mathbf{v} \times \mathbf{B} \ , \tag{2}$$

where p_e, n_e, and e are the electron pressure, number density, and charge respectively, and **v** is the fluid velocity. The curl of the isotropic pressure gradient is the familiar Biermann battery (or thermo-electric) term [17], driven by non-collinear temperature and density gradients. A Fourier analysis of the linearized equations by Nishiguchi [10] showed that RT-induced magnetic fields are $\pi/2$ out of phase with density modulations during linear growth as illustrated in Figure 1c. B-field generation and evolution are complex processes and a linear model is not sufficient to accurately describe the dynamics.

Numerical simulations are the common method used to calculate RT-induced magnetic fields under various conditions. In laser-ablated targets, acceleration of ablated material generates an RT-unstable region, perturbations
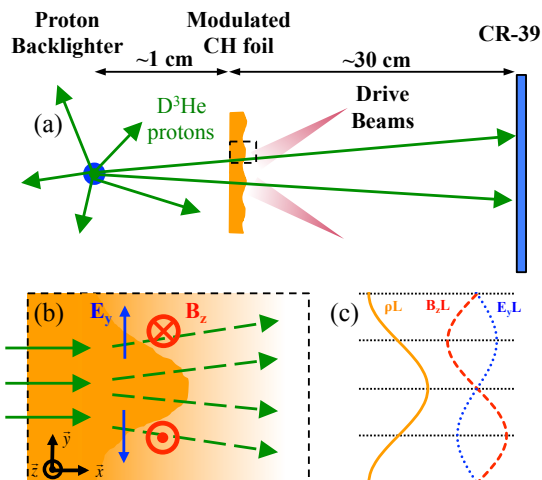

FIG. 1. (a) A schematic drawing of the experimental setup used to radiograph directly-driven plastic (CH) foils with 2D seed perturbations. Proton images are recorded on CR-39 nuclear track detectors. In x ray radiography experiments, a uranium foil backlighter was used, and images taken on film. (b) An expanded view of proton (green) deflections due to RT-induced density, E field (blue), and B field (red) modulations in the target. (c) Path-integrated quantities (arbitrary units) are shown during the linear growth phase.
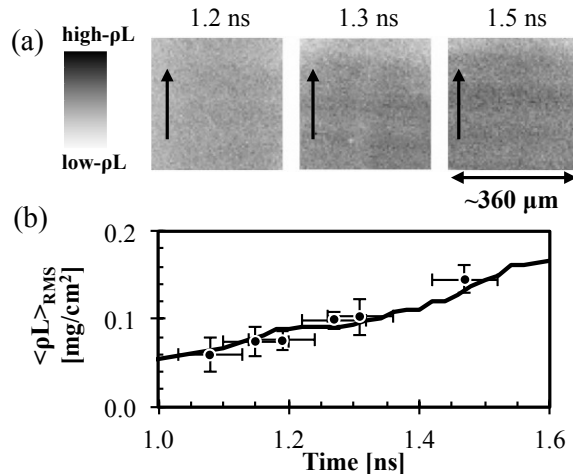
FIG. 2. (a) Sample x-ray radiographs of modulated targets at three times relative to the 2 ns laser drive; scale size is given in the target plane and the lineout direction is indicated. (b) Measured RMS areal densities (•) from x-ray radiographs and predicted values (solid) from DRACO.

will grow and induce magnetic fields. Separate calculations done by Mima *et al.* [9] and Nishiguchi *et al.* [10] were performed under different initial conditions, but both predicted $|B_{max}| \sim$10-100 T. Under conditions relevant to core-collapse supernovae, Fryxell *et al.* [8] predicted field strengths of $\sim$5 MG. A novel method for measuring these fields in planar targets was developed using a combination of proton and x ray radiography.

X ray radiographs provided measurements of density-modulation growth in CH targets. Face-on images were obtained using $\sim$1.3 keV x rays from a uranium backlighter and a streak camera [3, 19] having a temporal resolution of $\sim$80 ps and a spatial resolution of $\sim$10 μm. Sample x ray radiographs [20] are shown in Figure 2a. The RMS areal densities were calculated from lineouts of the radiographs and plotted in Figure 2b. These measurements demonstrate linear growth up to t$\sim$1.5 ns. For comparison, the 2D code DRACO [21, 22] simulated the radiative hydrodynamics of the RT growth using measured foil parameters and a constant flux limiter of 0.06. Predicted density modulations were benchmarked with x ray radiographs as shown by the solid line in Figure 2b. An exponential fit to RMS areal density measurements, independent of simulations, resulted in a growth rate of $\gamma \approx 2.2$ ns^{-1}.

Monoenergetic proton radiography [23, 24] was used to probe RT-induced field structures in laser irradiated CH foils. A thin-glass, exploding pusher filled with D^{3}He gas was imploded by 20 laser beams on the OMEGA laser. Monoenergetic fusion protons (15 MeV) were produced and broadened (3%) by thermal effects and by time-varying E fields around the implosion capsule when nuclear production occured during the laser pulse. [25] This backlighting technique provides a quasi-isotropic, monoenergetic proton source with an approximately Gaussian emission profile with FWHM$\sim$45 μm and burn duration of $\sim$150 ps, as demonstrated [26–29] in many experiments. The proton fluence image is recorded on 10 cm $\times$ 10 cm sheets of CR-39.

Proton radiographs of CH foils were taken over the course of three different shot days, providing data at different times during plasma evolution. Figure 3a shows sample proton fluence radiographs of both flat and modulated foils. [30] Radiographs were normalized for comparison across different experiments with the gray-scale set to $\pm$30% of the average fluence in each image. As expected, flat foils illustrate random behavior with no clear structure. However, coherent linear features are observed in radiographs of 2D modulated foils and lineouts are shown in Figure 3b. Proton fluence variation was quantified from individual lineouts of each radiograph.

A Discrete Fourier Transform (DFT) and resultant power spectrum[31] of each lineout were used to extract information at the known perturbation wavelength. The normalized RMS amplitude modulation was defined as $\alpha_{RMS} \equiv \sqrt{P_f/P_0}$, where P_f is the power density at the fundamental frequency of interest and P_0 is the power at zero frequency. This corresponds to the RMS of a sinusoid with frequency f normalized to the average. A Wiener Filter removes contributions to α_{RMS} from non-seed-perturbation effects, such as surface roughness of the foil and residual laser imprint. [19] Resulting α_{RMS} values are shown (▲) in Figure 3c and increase up to t$\sim$1.5 ns. Expected fluence modulations due to x ray measured density distributions of identical targets were calculated using the Monte Carlo code [32] Geant4 [33]. A model has been developed using the Geant4 framework to simulate proton scattering and was benchmarked against nonirradiated targets [35]. Amplitude modulations generated by proton scattering through x-ray measured density modulations are shown (•) in Figure 3c to be 3-5 times less than measurements.
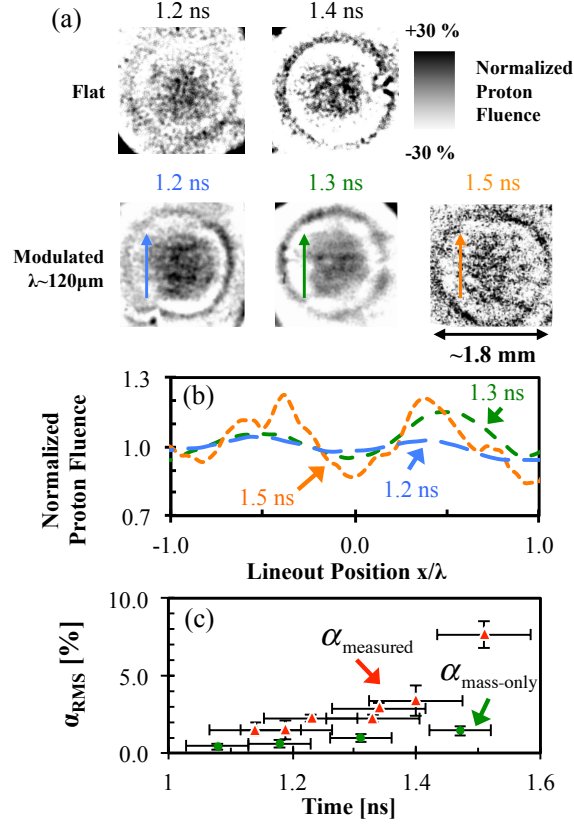
FIG. 3. (a) Sample proton fluence radiographs for flat and modulated foils; scale size is given in the target plane and lineout direction is indicated. Proton fluence is normalized for comparison across different shots. (b) Corresponding lineouts for radiographs of modulated targets. (c) Measured RMS fluence variations ($\blacktriangle$) in proton radiographs. Expected RMS variation due to mass only ($\bullet$) was calculated using density distributions from x-ray data.

The total amplitude modulation in proton fluence is due to a combination of perturbing effects from both field deflections and Coulomb scattering, $\alpha_{RMS}^2 = \alpha_{B/E}^2 + \alpha_{mass}^2$. The Coulomb scattering component was assessed from the x-ray inferred density modulations and shown to be small. The amount of deflection undergone by a proton caused by B or E fields is proportional to the path-integrated field strength; $\theta_B \propto \int B_\perp dl$, $\theta_E \propto \int E_\perp dl$, where $\perp$ indicates the component perpendicular to the proton trajectory. As a result, information regarding path-integrated field strength is encoded within proton fluence modulations. RT-induced modulations cause local broadening of the proton fluence due to Coulomb scattering and the Lorentz force, as illustrated in Figure 1b. Fluence perturbations in the center of proton radiographs are primarily due to field structures at the fundamental frequency of the perturbation wavelength.

The mass contribution to α_{RMS} was removed, and the residual attributed to deflections due to RT-induced magnetic and/or electric fields, $\alpha_{B/E} = \sqrt{\alpha_{RMS}^2 - \alpha_{mass}^2}$. Assuming a sinusoidally varying field during linear growth, as in the Nishiguchi model[10], expected $\alpha_{B/E}$ values were mapped to path-integrated field values. [34] RMS magnetic fields ($<BL>_{RMS}$) or electric fields ($<EL>_{RMS}$) were inferred from proton fluence modulation measurements by attributing residual amplitude modulation to *only magnetic fields* (Figure 4a) or *only electric fields* (Figure 4b). To determine whether B or E dominates proton deflection at the target, a simple model for estimating field strengths was implemented.

Magnetic and electric field evolution are described in the ideal MHD limit by Equations 1 and 2. Because magnetic Reynolds numbers are large ($\text{Re}_m \sim 100\text{-}1000$) [36] during laser illumination, magnetic diffusion may be neglected and an ideal MHD treatment is sufficient, though represents an approximate upper estimate of B field strength. In this limit, B field evolution is described by Equation 1 and is analogous to the fluid vorticity equation [37]. Therefore, the B field is found to be proportional to the fluid vorticity, $\mathbf{B} \propto \nabla \times \mathbf{v}$. Using the hydrodynamic predictions from DRACO, B field distributions were computed. E fields were then calculated by Equation 2 using the electron pressure and number density distributions from DRACO in conjunction with computed B fields. Simulated B and E fields
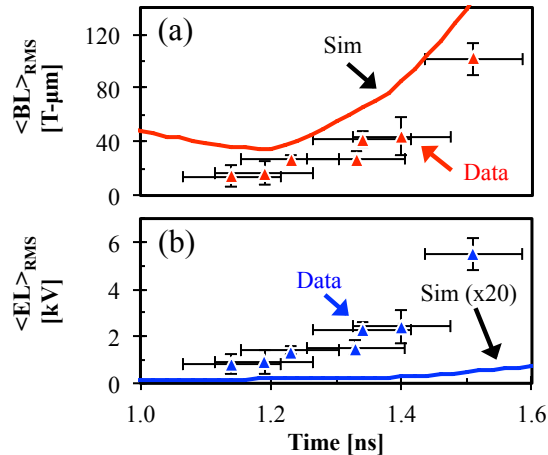
FIG. 4. Inferred path-integrated quantities (▲) are calculated from measured α_{RMS} values if deflections are caused by (a) B-fields and mass, or (b) E-fields and mass. Simulated B fields indicate an approximate upper estimate and are a factor of $\sim$2 higher than inferred values, whereas simulated E fields are a factor of $\sim$100 too low to account for measured proton fluence modulations.

were integrated in the direction of proton propagation up to the critical surface and RMS path-integrated field values were calculated for comparison with measured proton data.

Path-integrated B and E field estimates are shown by solid lines in Figure 4. Predicted $<BL>_{RMS}$ values were found to be higher than measurements by a factor of $\sim$2, but predicted $<EL>_{RMS}$ values were found to be low by a factor of $\sim$100. It should be noted that these calculations do not include Nernst convection [38], which may enhance the magnetic field strength. Though at the sampled times, measurements show that even an ideal MHD treatment slightly over estimates the field strength. Despite simplifications in this model, path-integrated field estimates indicate that proton deflections are dominantly due to magnetic, not electric, fields.
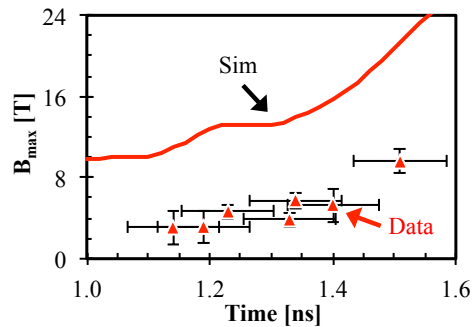

FIG. 5. B field amplitudes inferred from path-integrated measurements. The scale length of the field structure in the direction of proton propagation is approximated as the amplitude of the perturbation at each sample time.

Magnetic field magnitudes were estimated from path-integrated measurements using the peak-to-valley perturbation height as a scale size for field structure. The initial perturbation height at t=0 was $h_0 \approx 0.54$ μm and grows exponentially as $h \approx h_0 e^{\gamma t}$ where, from x ray measurements, $\gamma \approx 2.2$ ns^{-1}. Magnetic field amplitudes are computed as $B_{max} \approx \sqrt{2}$ $<BL>_{RMS}/h$ and shown in Figure 5 (the factor $\sqrt{2}$ relates RMS to peak amplitude for sinusoidal functions). Resultant B field amplitude estimates increase from $\sim$3 to $\sim$10 T during the linear growth phase and are $\sim$2-3 times lower than the simulated values. In these experiments, electron temperatures and densities near the ablation surface are estimated from simulations to be a few hundred eV and a few $\sim$10^{22} cm^{-3}, respectively. Under these conditions, the magnetic fields caused by $\lambda \approx 120$ μm perturbations result in a plasma β (ratio of fluid pressure to magnetic pressure) of $\sim$10^4, indicating a negligible effect on the local hydrodynamics. This conclusion will hold despite the scale-size-estimate uncertainty ($\sim$factor of a few). However, these fields increase in time and may affect the growth behavior later in time. Furthermore, as small-scale turbulent structures become more prevalent, strong magnetic fields may be generated, but are not observed in these data.

In summary, the first measurements of RT-induced magnetic fields generated by the Biermann battery were reported. X ray radiographs were used to measure density modulations in laser-irradiated 21 μm thick CH targets with imposed sinusoidal perturbations of wavelength $\lambda \approx 120$ μm and initial amplitudes of $a_0 \approx 0.27$ μm. Using monoenergetic proton radiography, images were taken of foils at select times during the linear phase of RT growth. It was shown that proton deflections due to RT-induced field structures are dominated by magnetic, not electric, fields. After compensating for proton scattering due to measured density modulations, path-integrated B fields were inferred from proton fluence radiographs and found to increase from ~ 10 to ~ 100 T-μm. These measurements illustrate the first experimental evidence of magnetic field generation due to the RT instability as predicted by numerical simulations in both astrophysical contexts as well as ICF. Observations made herein motivate further investigation of RT-induced magnetic field structures in different regimes using proton radiography.

* also at the Dept. of Mechanical Engineering and Physics
† now at State University of New York, Geneseo
‡ now at Lawrence Livermore National Laboratories
[1] J. W. Strutt. Proc London Math Soc, **14**, 8 (1883).
[2] G. Taylor. Proc Roy Soc of London, **201**, 192 (1950).
[3] V. A. Smalyuk, et al. Phys Plasma, **15**, 082703 (2008).
[4] J. D. Lindl, et al. Phys Plasma, **11**, 339 (2004).
[5] C. C. Joggerst, et al. Ap J, **723**, 11 (2010).
[6] H. Isobe, et al. Nature, **434**, 478 (2005).
[7] A. Schluter et al. Zeit Nat Teil A, **5**, 237 (1950).
[8] B. Fryxell, et al. High En Dens Phys, **6**, 162 (2010).
[9] K. Mima, et al. Phys Rev Lett, **41**, 1715 (1978).
[10] A. Nishiguchi. Japan J App Phys, **41**, 326 (2002).
[11] B. Srinivasan, et al. Phys Rev Lett, **accepted** (2012).
[12] T. R. Boehly, et al. Opt Comm, **133**, 495 (1997).
[13] S. P. Regan, et al. J. Opt. Soc. Am. B, **17**, 1483 (2000).
[14] T. R. Boehly, et al. J App Phys, **85**, 3444 (1999).
[15] Y. Lin, et al. Opt. Lett., **20**, 764 (1995).
[16] J. A. Stamper, et al. Phys Rev Lett, **26**, 1012 (1971).
[17] M. G. Haines. Can J Phys, **64**, 912 (1986).
[18] S. I. Braginskii. *Transport processes in a plasma*, volume 1 of *Reviews of Plasma Physics*. Consutants Bureau, New York (1965).
[19] V. A. Smalyuk, et al. Rev Sci Inst, **70**, 647 (1999).
[20] X ray data shown from OMEGA shot 50870.
[21] D. Keller, et al. *DRACO—A New Multidimensional Hydrocode* (1999).
[22] P. B. Radha, et al. Phys Plasma, **12**, 032702 (2005).
[23] C. K. Li, et al. Phys Plasma, **16**, 056304 (2009).
[24] C. K. Li, et al. Phys Rev Lett, **97**, 135003 (2006).
[25] C. K. Li, et al. Phys Plasma, **7**, 2578 (2000).
[26] F. H. Séguin, et al. Physics of Plasmas, **19**, 12 (2012).
[27] J. R. Rygg, et al. Science, **319**, 1223 (2008).
[28] C. K. Li, et al. Phys Rev Lett, **100**, 225001 (2008).
[29] R. D. Petrasso, et al. Phys Rev Lett, **103**, 085001 (2009).
[30] Proton radiographs from OMEGA shots 50610 (both flat images), 49109 (1.2 ns), 61721(1.3 ns), 49111(1.5 ns).
[31] W. H. Press, et al. *Numerical Recipes in C++: The Art of Scientific Computing Second Edition*. Cambridge Universtiy Press, 2 edition (2002).
[32] Geant4 uses a cold-matter approximation.
[33] J. Allison, et al. IEEE Trans Nuc Sci, **53**, 270 (2006).
[34] M. J.-E. Manuel, et al. Phys Plasma, **to be sub.** (2012).
[35] M. J.-E. Manuel, et al. Rev Sci Instr, **submitted** (2012).
[36] C. K. Li, et al. Phys Rev Lett, **99**, 055001 (2007).
[37] R. G. Evans. Plasma Phys Cont Fus, **28**, 1021 (1986).
[38] A. Nishiguchi, et al. Phys Rev Lett, **53**, 262 (1984).